High-Resolution Wide-Swath IRCI-Free MIMO SAR

High Resolution Wide Swath IRCI-Free MIMO SAR

Mohammed AlShaya, *Student Member, IEEE,* Mehrdad Yaghoobi, *Member, IEEE,* and Bernard Mulgrew, *Fellow, IEEE*

***Abstract*—A frequency domain system identification based multiple-input multiple-output (FDSI-MIMO) SAR algorithm using multiple phase centre multiple azimuth beams is proposed to obtain high resolution wide swath (HRWS) imaging. Frequency division multiple access (FDMA) is used in such a way that each transmitter emits a conventional linear frequency modulated (LFM) waveform modulated by a different carrier frequency and the obtained range resolution corresponds to the total transmitted bandwidth. In this paper, MIMO SAR problem is modelled, using the principle of displaced phase centre (DPC), as multiple but separate multiple-input single-output (MISO) system identification problems. The channel impulse responses of the individual MISO problems are identified in the range dimension using an FDSI-based estimation algorithm in such a way that the estimated range profile is free of inter-range cell interference (IRCI). In addition, the proposed algorithm does not require separating the sub-band waveforms at the receiver as they are processed jointly without a need to add guard bands between the adjacent sub-bands which would allow to utilise the available bandwidth to the maximum efficiency. The method of synthesising a wide transmit antenna beam from a narrow antenna beam applied in single-input multiple-output (SIMO) SAR is extended to MIMO SAR to remove the side-lobes effects of the receive beams and hence, leading to the desired signal to noise ratio (SNR). A pulse repetition frequency (PRF) lower than the Doppler bandwidth is used to obtain wide swath without experiencing aliasing in the Doppler spectrum. Finally, both simulated and constructed raw data are used to validate the effectiveness of the proposed algorithm.**

***Index Terms*—MIMO, system identification, LFM, SAR, Radar**

I. Introduction

SIMO SAR [1] and MIMO SAR [2] [3] [4] have been proposed to address the trade-off between the desired wide swath width and high cross-range resolution in conventional strip-map SAR. Single phase centre multiple azimuth beam (SPCMAB) SIMO SAR is proposed in [5] [6] [7] in which multiple azimuth receiving beams having a single phase centre but with different squint angles are formed. Wide Doppler bandwidth is synthesised from the Doppler spectra of the receiving azimuthal echo signals. MIMO SAR has been first introduced in [8] where it is stated that it is possible to obtain a high resolution wide swath image due to the extra phase centres introduced by the use of the multiple transmitters along with the multiple receiving channels. MIMO SAR can be used for ground moving target indication (GMTI) because of the availability of multiple antennas along the azimuth dimension [9].

Multiple sub-band MIMO SAR emits multiple radar waveforms with different carrier frequencies simultaneously [7]. This would allow to increase the transmitted bandwidth significantly. This type of MIMO SAR is mainly used to improve the range resolution instead of obtaining more effective phase centres in the azimuth than that of SIMO SAR.

The most challenging issue in MIMO radar is the design of multiple orthogonal waveforms in such a way that the waveforms are orthogonal to each other regardless of the time delays and Doppler shifts [10]. The authors in [11] [12] use up and down-chirps to generate a more sophisticated waveform consisting of a sequence of multiple sub-pulses in such a way that each sub-pulse is simply a superposition of multiple chirped signals. Short-term shift orthogonal waveforms are proposed in [10] which uses digital beamforming on receive in elevation to suppress distant scatterers.

A detailed analysis of different MIMO radar waveforms is provided in [13]. According to the analysis, time division multiple access (TDMA) waveforms are perfectly orthogonal but this approach suffers from a significant loss of the transmit power. For code division multiple access (CDMA) waveforms, it is not possible to obtain good auto and cross-correlation properties in a single sequence. In frequency division multiple access (FDMA) waveforms, each transmit antenna transmits at different carrier frequency. The mere use of FDMA waveforms (i.e. without processing the sub-band waveforms jointly) will restrict the range resolution to correspond to the bandwidth of a single transmitting waveform (i.e. sub-band waveform) [14] [15].

An inter-range cell interference (IRCI) free based on cyclic prefix (CP) orthogonal frequency division multiplexing (OFDM) waveform is proposed in [16] but the use of cyclic prefix, which is removed at the receiver, does not allow the full utilisation of the transmitted energy. In addition, the length of the pulse width should be at least equal to the length of the channel to be estimated which is not practical in some applications such as strip-map SAR. The same authors proposed in [17] an algorithm to make most of the cyclic prefix zeros to solve the problem of energy efficiency but introduced a trade-off between having a constant modulus waveforms in the frequency domain and low peak to average power ratio (PAPR) waveforms.

Most of sub-bands MIMO-SAR algorithms in the literature [18] [19] use a bank of band pass filters (BPFs) at the receiver to separate the sub-bands. However, the overlapping between the adjacent sub-bands will affect the performance of the range profile estimation. Therefore, a guard band needs to be added between the adjacent sub-bands so that they can be separated at the receiver using a bank of BPFs [19] which would affect

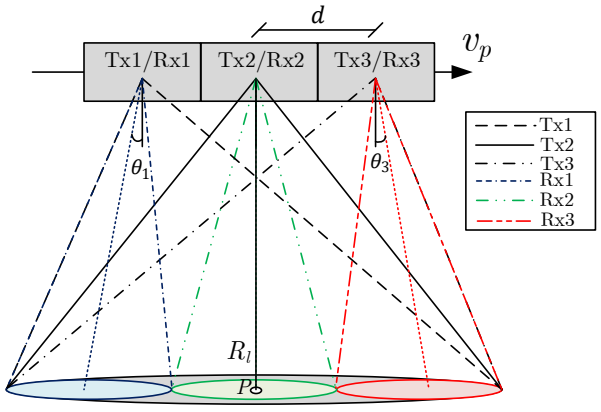

Fig. 1. MIMO SAR configuration where R_l is the slant range of the closest approach to a point target P located at the l^{th} range cell, v_p is the platform velocity, d is the distance between adjacent Tx/Rx and θ_n is the squint angle of the n^{th} receiver beam ($\theta_2 = 0$).

the bandwidth utilisation efficiency.

In this paper, we propose a new MIMO SAR configuration shown in Fig.1 in which the beams of the transmitters are wide and multiple adjacent receiving sub-beams with different phase centres and squint angles are generated in the azimuth direction. The system pulse repetition frequency (PRF) needs only to satisfy the Nyquist rate of the partial Doppler bandwidth corresponding to each receiver sub-beam. Wide Doppler bandwidth is then synthesised to obtain wide swath high resolution image. In addition, we propose a frequency domain system identification (FDSI) based algorithm to estimate the channel impulse response in the range dimension instead of a matched filter which has the property of ideally having a zero side-lobes level, IRCI-free property, and the length of the transmitted waveform is not function of the channel impulse response length in the range dimension.

Moreover, our proposed algorithm does not require separating the sub-bands at the receiver as they are processed jointly without a need to add guard bands between adjacent sub-bands. As a result, the proposed algorithm utilises the available bandwidth to the maximum efficiency and facilitates the use of LFM waveforms and hence gains all the inherent benefits of these waveforms (e.g. constant envelope and unity peak to average power). The narrowband assumption is relaxed to the bandwidth of the individual transmitted sub-band as FDMA is used.

Finally, we extend the method of synthesising a wide transmit antenna beam from a narrow antenna beam applied in SIMO SAR to MIMO SAR in order to attain the desired SNR. Some initial results of an FDSI based algorithm was reported in [20].

Notations. Matrices are denoted by upper case bold letters (e.g. $\mathbf{A}$) while scalars and vectors are denoted by upper\lower case letters (e.g. a and A) and bold lower case letters (e.g. $\mathbf{a}$), respectively. In addition, $(.)^T$ and $(.)^H$ denote the transpose and hermitian operators, respectively. $\text{diag}(\mathbf{a})$ denotes a matrix with the vector $\mathbf{a}$ as main diagonal. $\mathcal{C}$ represents the field of complex numbers.

II. MIMO SAR System Model

The following section starts with the derivation of the received signal model of MIMO SAR, in a way independent of the transmitted waveforms. The MIMO SAR problem is then formulated as an N individual multiple-input single-output (MISO) system identification problems using the principle of displaced phase centre (DPC) where N is the number of receivers. A frequency domain system identification (FDSI) based estimation algorithm is then derived to estimate the channel impulse response of the individual MISO problems. The estimated channel responses are then combined in the azimuth dimension to obtain a high resolution wide swath (HRWS) image.

A. Received Signal Model

Consider a narrowband MIMO radar system with an array of M antenna elements at the transmitter and an array of N antenna elements at the receiver. A set of M known sub-band waveforms (i.e. LFM waveforms) $\mathbf{x}(t) \in \mathcal{C}^{M\times 1}$ in which each occupies a portion of the total transmitting bandwidth are emitted through the transmitting array and can be defined as

$$\mathbf{x}(t) = [x_1(t), x_2(t), ..., x_M(t)]^T \tag{1}$$

The baseband received signal at the n^{th} receive antenna can be expressed as

$$y_n(t,\eta) = \sum_{m=1}^{M}\sum_{l=0}^{L-1} \sigma_l e^{-j2\pi F_c \tau_{l,mn}(\eta)} x_m(t-\tau_{l,mn}(\eta)) + w_n(t) \tag{2}$$

where t and η denote the fast time and slow time, respectively. F_c denotes the carrier frequency, $x_m(t)$ is the m^{th} transmitted waveform, σ_l is the radar cross-section (RCS) of the scattering point located at the l^{th} range cell of the swath, $\tau_{l,mn}(\eta)$ is the round trip delay of the l^{th} scattering point when the waveform is transmitted by the m^{th} transmitter and received by the n^{th} receiver and $w_n(t)$ is additive white noise generated by the n^{th} receiver.

Without loss of generality, consider the case when $M = N = 3$ as shown in Fig.1. The received signals at the receivers can be expressed as the following ($\forall n = 1, 2, 3$),

$$\begin{aligned} y_n(t,\eta) = &\sum_{l=0}^{L-1} \sigma_l e^{-j2\pi F_c \tau_{l,1n}(\eta)} x_1(t-\tau_{l,1n}(\eta)) + \\ &\sum_{l=0}^{L-1} \sigma_l e^{-j2\pi F_c \tau_{l,2n}(\eta)} x_2(t-\tau_{l,2n}(\eta)) + \\ &\sum_{l=0}^{L-1} \sigma_l e^{-j2\pi F_c \tau_{l,3n}(\eta)} x_3(t-\tau_{l,3n}(\eta)) + w_n(t) \end{aligned} \tag{3}$$

where,

$$\tau_{l,mn}(\eta) = \frac{R_{l,m}(\eta) + R_{l,n}(\eta)}{c}, \quad \forall m, n = 1, 2, 3 \tag{4}$$

$R_{l,m}$ and $R_{l,n}$ are the slant range from the m^{th} transmitter to the l^{th} scattering point and from the n^{th} receiver to the l^{th} scattering point, respectively, and can be expressed under the assumption of a straight sensor trajectory and approximated using Taylor expansion to the second order as the following [9],

$$\begin{aligned} R_{l,n}(\eta) =& \sqrt{R_l^2 + (v_p\eta + (2-n)d)^2 - 2R_l v_p \eta \sin(\theta_n)} \\ &\approx R_l - v_p \sin(\theta_n)(\eta + (2-n)\frac{d}{v_p}) + \\ &\frac{v_p^2 \cos^2(\theta_n)(\eta + (2-n)d/(v_p))^2}{2R_l} \end{aligned} \tag{5}$$

where v_p is the platform velocity, θ_n denotes the squint angle of the n^{th} receiver and R_l is the slant range to the l^{th} scatterer when $\eta = 0$ (i.e. the slant range of the closest approach). Quadratic approximation of $R_{l,m}(\eta) + R_{l,n}(\eta)$ can be expressed as the following (see Appendix A for the derivation),

$$R_{l,m}(\eta) + R_{l,n}(\eta) \approx 2R_{l,m}(\eta - \frac{\Delta y_{mn}}{2v_p})_{\theta=\theta_n} + \frac{\Delta y_{mn}^2}{4R_l} \tag{6}$$

where Δy_{mn} denotes the separation between the m^{th} transmitter and the n^{th} receiver. The azimuth impulse response $h_{az,mn}$ when the signal is transmitted by the m^{th} transmitter and received by the n^{th} receiver is determined by the distance of the transmit and receive path which can be expressed as

$$h_{az,mn}(\eta) = e^{-j\frac{2\pi}{\lambda}(R_{l,m}(\eta)+R_{l,n}(\eta))} \tag{7}$$

It can be seen from (6) and (7) that the principle of the displaced phase centre (DPC) [9] holds which can be used to express the following,

$$h_{az,12}(\eta) = h_{az,22}(\eta + \frac{d}{2v_p})e^{-j\frac{\pi d^2}{2\lambda R_l}} \tag{8}$$

$$h_{az,21}(\eta) = h_{az,11}(\eta - \frac{d}{2v_p})e^{-j\frac{\pi d^2}{2\lambda R_l}} \tag{9}$$

$$h_{az,32}(\eta) = h_{az,22}(\eta - \frac{d}{2v_p})e^{-j\frac{\pi d^2}{2\lambda R_l}} \tag{10}$$

$$h_{az,23}(\eta) = h_{az,33}(\eta + \frac{d}{2v_p})e^{-j\frac{\pi d^2}{2\lambda R_l}} \tag{11}$$

$$h_{az,13}(\eta) = h_{az,22}(\eta)e^{-j\frac{2\pi d^2}{\lambda R_l}} \tag{12}$$

The received signal in (3) is sampled from the range cell that corresponds to the near range to the range cell that corresponds to the far range with a sampling frequency of $f_s = 1/T_s$. The signals are also sampled in the azimuth dimension with a sampling frequency of $f_p = \text{PRF}$ which is the pulse repetition frequency. The discrete time version of the received signal can be expressed as the following ($\forall n = 1, 2, 3$),

$$\begin{aligned} z_n[n_t, n_a] =& \\ &\sum_{l=0}^{L-1} h_{1n}[l, n_a]x_1[n_t - l] + \sum_{l=0}^{L-1} h_{2n}[l, n_a]x_2[n_t - l] \\ &\sum_{l=0}^{L-1} h_{3n}[l, n_a]x_3[n_t - l] + w_n[n_t] \end{aligned} \tag{13}$$

where,

$$\begin{aligned} h_{mn}[l, n_a] =& \sigma_l e^{-j2\pi F_c \tau_{l,mn}(n_a)} \\ =& \sigma_l e^{j\phi_{l,mn}(n_a)} \end{aligned} \tag{14}$$

n_t and n_a are the range and azimuth time indices, respectively.

B. Impulse Response Estimation and Image Formation

As described previously, each transmitter emits a portion of the total bandwidth and the range resolution should correspond to the total transmitted bandwidth. Therefore, the received signals due to all the transmitted waveforms should be processed jointly. In addition, the effective sampling frequency in the azimuth dimension is $\text{PRF} = B_d/N$ where B_d is the Doppler bandwidth so it is expected to have an azimuth ambiguity. The azimuth ambiguity is avoided by reducing the beamwidth of each receiver so that the Doppler bandwidth of each receiver is B_d/N. The beam of each receiver should have a squint angle so that the area spotted by the wide transmitted beams are completely covered as shown in Fig.1. The cross-range resolution should correspond to the full Doppler bandwidth B_d and thus, the Doppler bandwidths at all receivers should be processed jointly as explained next.

The Fourier transform of (13) across both azimuth and range dimensions (for $n = 1, 2, 3$), expressed as a function of the impulse response whose phase centre is located in the middle using the principle of DPC (8)-(12), can be written as the following,

$$\begin{aligned} Z_1(f_r, f_a) =& X_1(f_r)H_{11}(f_r, f_a) + X_2(f_r)H_{21}(f_r, f_a) + \\ & X_3(f_r)H_{31}(f_r, f_a) + W_1(f_r) \\ =& B_1(f_r, f_a)H_{31}(f_r, f_a) + W_1(f_r) \end{aligned} \tag{15}$$

$$\begin{aligned} Z_2(f_r, f_a) =& X_1(f_r)H_{12}(f_r, f_a) + X_2(f_r)H_{22}(f_r, f_a) + \\ & X_3(f_r)H_{32}(f_r, f_a) + W_2(f_r) \\ =& B_2(f_r, f_a)H_{22}(f_r, f_a) + W_2(f_r) \end{aligned} \tag{16}$$

$$\begin{aligned} Z_3(f_r, f_a) =& X_1(f_r)H_{13}(f_r, f_a) + X_2(f_r)H_{23}(f_r, f_a) + \\ & X_3(f_r)H_{33}(f_r, f_a) + W_3(f_r) \\ =& B_3(f_r, f_a)H_{13}(f_r, f_a) + W_3(f_r) \end{aligned} \tag{17}$$

where,

$$\begin{aligned} &B_1(f_r, f_a) = \\ &X_1(f_r)e^{j\frac{2\pi df_a}{v_p}}e^{j\frac{2\pi d^2}{\lambda R_l}} + X_2(f_r)e^{j\frac{\pi df_a}{v_p}}e^{j\frac{3\pi d^2}{2\lambda R_l}} + X_3(f_r) \end{aligned} \tag{18}$$

$$\begin{aligned} &B_2(f_r, f_a) = \\ &X_1(f_r)e^{j\frac{\pi df_a}{v_p}}e^{-j\frac{\pi d^2}{2\lambda R_l}} + X_2(f_r) + X_3(f_r)e^{-j\frac{\pi df_a}{v_p}}e^{-j\frac{\pi d^2}{2\lambda R_l}} \end{aligned} \tag{19}$$

$$\begin{aligned} &B_3(f_r, f_a) = \\ &X_1(f_r) + X_2(f_r)e^{-j\frac{\pi df_a}{v_p}}e^{j\frac{3\pi d^2}{2\lambda R_l}} + X_3(f_r)e^{-j\frac{2\pi df_a}{v_p}}e^{j\frac{2\pi d^2}{\lambda R_l}} \end{aligned} \tag{20}$$

The spectra of the transmitting waveforms $X_m(f_r)$ $\forall m \in [1, 2, 3]$ from (18), (19) and (20) are chosen such that each $B_n(f_r, f_a)$ $\forall n \in [1, 2, 3]$ occupies the whole fast

time spectrum to identify $H_{31}(f_r, f_a)$, $H_{22}(f_r, f_a)$ and $H_{13}(f_r, f_a)$. The impulse responses $H_{31}(f_r, f_a)$, $H_{22}(f_r, f_a)$ and $H_{13}(f_r, f_a)$ will be estimated individually using the FDSI algorithm proposed in [21]. All of the estimated impulse responses have the same phase centre but each occupies a portion of the Doppler bandwidth. Therefore, they need to be analysed in order to synthesise the full Doppler bandwidth properly to obtain the corresponding cross-range resolution in the formed image.

The instantaneous Doppler frequency of $h_{31}[l, n_a]$, $h_{22}[l, n_a]$ and $h_{13}[l, n_a]$ can be derived as the following,

$$\begin{aligned} f_{d,31}(n_a) &= \frac{1}{2\pi}\frac{d}{dn_a}\phi_{l,31}(n_a) \\ &= \underbrace{\frac{2}{\lambda}v_p\sin(\theta_1)}_{f_{dc,31}} - \frac{2}{\lambda}\frac{v_p^2\cos^2(\theta_1)n_aT_r}{R_l} \end{aligned} \tag{21}$$

$$\begin{aligned} f_{d,22}(n_a) &= \frac{1}{2\pi}\frac{d}{dn_a}\phi_{l,22}(n_a) \\ &= \underbrace{\frac{2}{\lambda}v_p\sin(\theta_2)}_{f_{dc,22}} - \frac{2}{\lambda}\frac{v_p^2\cos^2(\theta_2)n_aT_r}{R_l} \end{aligned} \tag{22}$$

$$\begin{aligned} f_{d,13}(n_a) &= \frac{1}{2\pi}\frac{d}{dn_a}\phi_{l,13}(n_a) \\ &= \underbrace{\frac{2}{\lambda}v_p\sin(\theta_3)}_{f_{dc,13}} - \frac{2}{\lambda}\frac{v_p^2\cos^2(\theta_3)n_aT_r}{R_l} \end{aligned} \tag{23}$$

where T_r denotes the pulse repetition interval, θ_n denotes the squint angle of the n^{th} receiver and $f_{dc,mn}$ is the Doppler centroid of h_{mn}. As the squint angles of the receivers are generally small, it can be seen from (21), (22) and (23) that the Doppler bandwidth of each receiver can be expressed as the following,

$$B_{d,13} \approx B_{d,22} \approx B_{d,31} = \left|\frac{2}{\lambda}\frac{v_p^2\cos^2(\theta_1)T_a}{R_l}\right| \tag{24}$$

where T_a is the synthetic aperture time. Without loss of generality, chirp scaling (CS) algorithm is used for image formation [22]. The estimation of $H_{31}(f_r, f_a)$ will be now considered and the same process will be applied to estimate $H_{22}(f_r, f_a)$ and $H_{13}(f_r, f_a)$.

The first phase function of the chirp scaling algorithm equalises all range migration trajectories to a reference range r_{ref} by multiplying (15) in the range-Doppler domain with the following,

$$\begin{aligned} z_{s,1}(n_t, f_a) &= z_1(n_t, f_a)H_{\text{CS},1}(n_t, f_a) \\ &= z_1(n_t, f_a)\exp\Big[j\pi k(f_a; r_{\text{ref}})a(f_a) \\ &\times \big(n_tT_s - \frac{2R(f_a; r_{\text{ref}})}{c}\big)^2\Big] \end{aligned} \tag{25}$$

where,

$$R(f_a; r_{\text{ref}}) = \frac{r_{\text{ref}}}{\beta(f_a)} = r_{\text{ref}}(1 + a(f_a)), \tag{26}$$

$$\frac{1}{k(f_a; r_{\text{ref}})} = \frac{1}{k_r} - \frac{2\lambda r_{\text{ref}}(\beta^2(f_a) - 1)}{c^2\beta^3(f_a)}, \tag{27}$$

$$\beta(f_a) = \sqrt{1 - \left(\frac{f_a\lambda}{2v_p}\right)^2}, \tag{28}$$

$a(f_a)$ denotes the chirp scaling factor, k_r is the modulation rate of the transmitted chirps and the azimuth frequency f_a varies within the following range.

$$\frac{-\text{PRF}}{2} + f_{dc,31} \leq f_a \leq \frac{\text{PRF}}{2} + f_{dc,31} \tag{29}$$

The next step is to estimate the range impulse response at every Doppler frequency using our proposed FDSI algorithm in [21]. The scaled received signal in (25) can be re-expressed as the following,

$$\begin{aligned} z_{s,1}[n_t, f_a] = \sum_{l=0}^{L-1} h_{31}[l, f_a]b_{s,1}[n_t - l, f_a] + w_{s,1}[n_t, f_a] \\ 0 \leq n_t \leq K + L - 1 \end{aligned} \tag{30}$$

where K is the length of the waveform transmitted, $w_{s,1}[n_t, f_a]$ is the noise after being multiplied with $H_{\text{CS},1}$ in the range-Doppler domain and $b_{s,1}[n_t, f_a]$ is the combined transmitted chirps but with a new chirp rate which varies with the Doppler frequency as given below

$$k_{\text{CS}}(f_a) = k(f_a; r_{\text{ref}})(1 + a(f_a)) \tag{31}$$

The received signal in (30) can be written in a matrix form for a given Doppler frequency (f_a) as

$$\begin{aligned} \mathbf{z}_{s,1}(f_a) &= \big[z_{s,1}[0, f_a], z_{s,1}[1, f_a], ..., z_{s,1}[K + L - 1, f_a]\big]^T \\ &= \mathbf{B}_{s,1}(f_a)\mathbf{h}_{31}(f_a) + \mathbf{w}_{s,1}(f_a) \end{aligned} \tag{32}$$

where $\mathbf{h}_{31}(f_a) = \big[h_{31}[0, f_a], h_{31}[1, f_a], ..., h_{31}[L-1, f_a]\big]^T$, $\mathbf{w}_{s,1}(f_a) = \big[w_{s,1}[0, f_a], w_{s,1}[1, f_a], ..., w_{s,1}[K + L - 1, f_a]\big]^T$ and the matrix $\mathbf{B}_{s,1}(f_a)$ is of dimension $(K + L - 1) \times L$ which can be expressed as the following,

$$\mathbf{B}_{s,1}(f_a) = \begin{bmatrix} b_{s,1}[0, f_a] & 0 & \dots & \dots & 0 \\ b_{s,1}[1, f_a] & b_{s,1}[0, f_a] & & & 0 \\ \vdots & b_{s,1}[1, f_a] & \ddots & & \vdots \\ b_{s,1}[K-1, f_a] & \vdots & \vdots & \ddots & 0 \\ 0 & b_{s,1}[K-1, f_a] & & & b_{s,1}[0, f_a] \\ 0 & 0 & \ddots & \vdots & b_{s,1}[1, f_a] \\ \vdots & \vdots & & \ddots & \vdots \\ 0 & 0 & \dots & 0 & b_{s,1}[K-1, f_a] \end{bmatrix} \tag{33}$$

The matrix $\mathbf{B}_{s,1}(f_a)$ can be made circulant and accordingly, the channel impulse response $\mathbf{h}_{31}(f_a)$ in (32) is zero padded by $(K-1)$ as the following,

$$\mathbf{z}_{s,1}(f_a) = \mathbf{B}_{s,1C}(f_a)\underbrace{\begin{bmatrix}\mathbf{h}_{31}(f_a) \\ \mathbf{0}_{(K-1)}\end{bmatrix}}_{\mathbf{h}_{31,p}(f_a)} + \mathbf{w}_{s,1}(f_a) \tag{34}$$

Where $\mathbf{B}_{s,1C}(f_a)$ is as illustrated in Appendix B. The channel impulse response can be estimated as the following,

$$\hat{\mathbf{h}}_{31,p}(f_a) = \mathbf{B}_{s,1C}^{-1}(f_a)\mathbf{z}_{s,1}(f_a) \tag{35}$$

The estimation in (35) can be performed easily in the frequency domain by exploiting the DFT structure of $\mathbf{B}_{s,1C}(f_a)$ after being decomposed as the following,

$$\mathbf{B}_{s,1C}(f_a) = \mathbf{F}\text{diag}\{\mathcal{X}\}\mathbf{F}^H \tag{36}$$

where $\mathcal{X}$ is the Fourier transform of the first row of the matrix $\mathbf{B}_{s,1C}(f_a)$ and $\mathbf{F}$ is the DTFT matrix. It should be noted that the last $(K-1)$ elements of $\hat{\mathbf{h}}_{31,p}$ should be forced to be zero which can be seen as a noise removal step. The impulse response estimation described above should be performed for all Doppler frequencies.

The bulk range cell migration correction (RCMC) is then performed by multiplying (35) in range frequency-Doppler domain with a phase term expressed below

$$H_{\text{RCMC}}(f_r, f_a) = \exp\left[j4\pi r_{\text{ref}} a(f_a) f_r / c\right] \tag{37}$$

The same process is applied to estimate $\mathbf{h}_{22}(f_a)$ and $\mathbf{h}_{13}(f_a)$ for all Doppler frequencies. A constant phase term should be compensated for in the estimated $\mathbf{h}_{22}(f_a)$ to make sure that its phase centre is aligned with the phase centres of the other estimated impulse responses and this can be done by multiplying the estimated $\mathbf{h}_{22}(f_a)$ by the following constant phase,

$$H_{comp} = e^{-j\frac{2\pi d^2}{\lambda R_l}} \tag{38}$$

The full Doppler bandwidth is synthesised before forming the image by performing the following steps:

1) The data of each receiving beam after RCMC is converted into range time-Doppler domain.
2) The data of each receiving beam is then zero-padded in the Doppler dimension so that the points of each Doppler spectrum are increased by a factor of N.
3) Each zero-padded data is then frequency shifted in the Doppler dimension by the corresponding Doppler centroid to compensate for the Doppler shift introduced by the squint angle.
4) The data of all receiving beams are then added together to form the full Doppler bandwidth spectrum.

The resulted full Doppler bandwidth data in the range time-Doppler domain is multiplied by $H_{CS,2}$ defined below to compensate for the residual phase and perform azimuth compression.

$$H_{\text{CS},2}(n_t, f_d; r_{\text{ref}}) = \exp\left[\frac{j2\pi r_{\text{ref}}}{v_p}\sqrt{f_{am}^2 - f_d^2}\right] \times \exp[j\Delta\varphi(f_d, r_{\text{ref}})] \tag{39}$$

$$\Delta\varphi(f_d, r_{\text{ref}}) = \frac{4\pi}{c^2}k(f_d)a(f_d)(1+a(f_d))(r_0 - r_{\text{ref}})^2 \tag{40}$$

$$\frac{-N\text{PRF}}{2} \le f_d \le \frac{N\text{PRF}}{2} \tag{41}$$

where $f_{am} = 2v_p/\lambda$ and $r_0 = cn_tT_s/2$. The inverse azimuth Fourier transform is finally taken to obtain the image.

C. Transmitter Wide Beam Generation

The same antenna array can be used for both transmission and reception of the radar pulses by applying digital beamforming techniques. The trivial solution to synthesise wide transmit beam is the application of amplitude tapering but this would significantly reduce the radiated power [6]. In addition, the high-power amplifiers may not be driven in saturation which would lower the overall efficiency.

The wide transmit beam in Fig.1 can be achieved by transmitting multiple sub-pulses sequentially in a single pulse repetition interval (PRI) using the same narrow receive beam. Each transmitted sub-pulse is associated with a different transmit narrow beam which is switched in such a way that the wide transmit beam is synthesised as shown in Fig.2. This operation permits the use of the same large receive antenna which reduces the peak power requirement in order to attain the desired signal-to-noise ratio (SNR). Furthermore, the use of a synthesised wide beam will suppress the receiving inter-beams overlapping by employing digital beamforming (DBF) on receive in elevation which has been applied in modified SPCMB SAR [5] [23] [24] [25]. Echoes corresponding to different sub-pulses (at each instant of time) arrive from different elevation angles. Therefore, it is possible to separate them by digital beamforming on receive in elevation using the relation between time delay and elevation angle in a side-looking radar imaging geometry.

This operation has a disadvantage that the transmit window gets broadened because of the multiple transmitted sub-pulses in a single PRI which enlarges the blind area. However, it does not affect the application under consideration (i.e. HRWS imaging) which relies on a rather low PRF and the sub-pulse switching times which are of the order of several microseconds can be included without loosing much of the duty cycle [6].

A fractional delay t_d which includes the beam switching time as shown in Fig.2 should be accounted for in the range profile estimation. This can be done by re-expressing $B_1(f_r, f_a)$, $B_2(f_r, f_a)$ and $B_3(f_r, f_a)$ in (15),(16) and (17) as the following,

$$B_1(f_r, f_a) = X_1(f_r)e^{j\frac{2\pi df_a}{v_p}}e^{j\frac{2\pi d^2}{\lambda R_l}} + X_2(f_r)e^{j\frac{\pi df_a}{v_p}}e^{j\frac{3\pi d^2}{2\lambda R_l}} + X_3(f_r) \tag{42}$$

$$B_2(f_r, f_a) = \left(X_1(f_r)e^{j\frac{\pi df_a}{v_p}}e^{-j\frac{\pi d^2}{2\lambda R_l}} + X_2(f_r) + X_3(f_r)e^{-j\frac{\pi df_a}{v_p}}e^{-j\frac{\pi d^2}{2\lambda R_l}}\right)e^{-j2\pi f_r t_d} \tag{43}$$

$$B_3(f_r, f_a) = \left(X_1(f_r) + X_2(f_r)e^{-j\frac{\pi df_a}{v_p}}e^{j\frac{3\pi d^2}{2\lambda R_l}} + X_3(f_r)e^{-j\frac{2\pi df_a}{v_p}}e^{j\frac{2\pi d^2}{\lambda R_l}}\right)e^{-j4\pi f_r t_d} \tag{44}$$

Due to the different introduced delays present in (42)-(44), echoes corresponding to different sub-pulses (i.e. receiving beams) can be separated by digital beamforming on receive in elevation. The same process described in section II-B is then applied to estimate the impulse response and form the image.

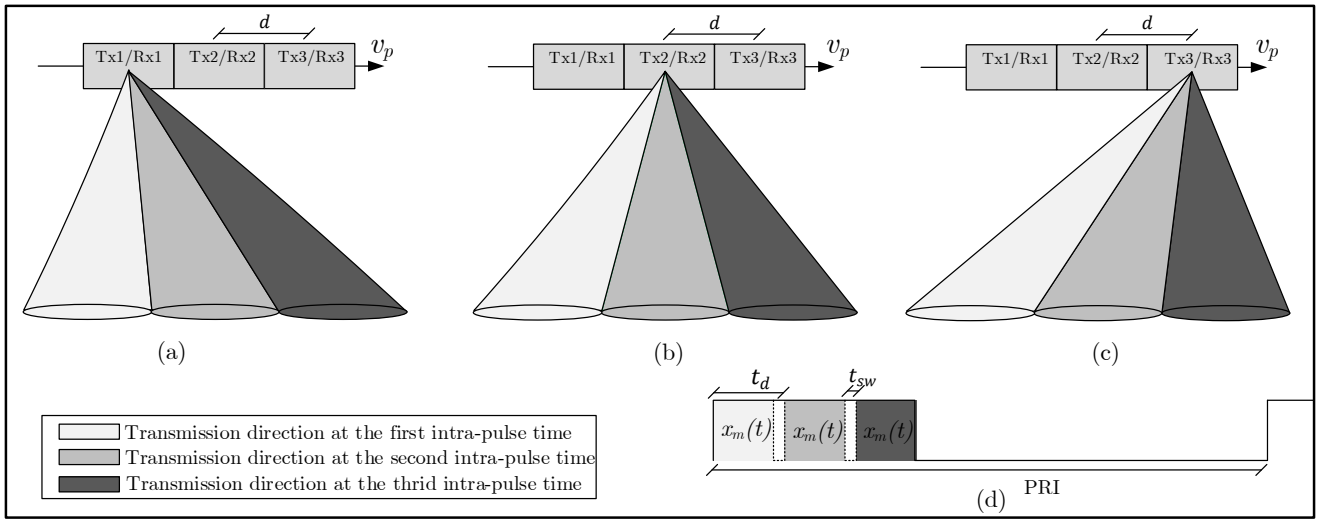

Fig. 2. Generation of synthesised wide transmission beams from narrow beams. (a) Transmission directions sequence of the $1^{\rm st}$ transmitter. (b) Transmission directions sequence of the $2^{\rm nd}$ transmitter. (c) Transmission directions sequence of the $3^{\rm rd}$ transmitter. (d) Timing structure of a single PRI transmitted by the $m^{\rm th}$ transmitter where t_{sw} denotes the beam switching time.

D. Azimuth Ambiguity Analysis

The azimuth beams of the receivers are not ideal and the side-lobes of the receive beams will overlap with the main-lobes of the adjacent azimuth beams. The azimuth ambiguity is similar to the one occurred in SPCMB-SAR [9] which is analysed next.

Without loss of generality, raised cosine function is used to generate the transmit and receive beam patterns in the azimuth ambiguity analysis. The transmitter beam is N times wider than any receive beam so that the one-way normalised azimuthal transmit and receive power patterns can be expressed as

$$G_t(\theta) = \left(\mathrm{sinc}\big(U_{Tx}(\theta)\big)\frac{\cos(\pi U_{Tx}(\theta))}{1-4(U_{Tx}(\theta))^2}\right)^2 \tag{45}$$

$$G_{r,n}(\theta) = \left(\mathrm{sinc}\big(U_{Rx,n}(\theta-\theta_n)\big)\frac{\cos(\pi U_{Rx,n}(\theta-\theta_n))}{1-4(U_{Rx,n}(\theta-\theta_n))^2}\right)^2 \tag{46}$$

where,

$$U_{Tx}(\theta) = \frac{\pi L_a}{N\lambda}\sin(\theta), \tag{47}$$

$$U_{Rx,n}(\theta) = \frac{\pi L_a\cos(\theta_n)}{\lambda}\sin(\theta) \tag{48}$$

for $(n = 0, 1, 2, ..., N)$. θ_n and L_a denote the squint angle of the $n^{\rm th}$ receiver and the antenna azimuth length of the receiver, respectively. The normalised equivalent combined power pattern of the broad transmit beam and the $n^{\rm th}$ narrow receive beam can be expressed as the following,

$$G_n(\theta) = \left(\mathrm{sinc}\big(U_{Tx}(\theta)\big)\frac{\cos(\pi U_{Tx}(\theta))}{1-4(U_{Tx}(\theta))^2}\right)\times \left(\mathrm{sinc}\big(U_{Rx,n}(\theta-\theta_n)\big)\frac{\cos(\pi U_{Rx,n}(\theta-\theta_n))}{1-4(U_{Rx,n}(\theta-\theta_n))^2}\right) \tag{49}$$

The 3-dB width of the combined pattern in (49) is 30% wider than the narrow receive beam [26] which is not the case when synthesising wide transmit beams using narrow beams. Therefore, the PRF should be 30% higher than the ideal case in order to achieve the desired azimuth ambiguity level. The azimuth ambiguity to signal ratio (AASR) for the $n^{\rm th}$ receive beam can be computed as the following,

$$\mathrm{AASR}_n = \frac{\sum_{\substack{k=-\infty\\k\neq 0}}^{\infty}\int_{(f_{dc,n}-0.5B_{d,\mathrm{Rx}})}^{(f_{dc,n}+0.5B_{d,\mathrm{Rx}})} G_n^2(f+kf_r)\mathrm{d}f}{\int_{(f_{dc,n}-0.5B_{d,\mathrm{Rx}})}^{(f_{dc,n}+0.5B_{d,\mathrm{Rx}})} G_n^2(f)\mathrm{d}f} \tag{50}$$

where $f_{dc,n}$ is the Doppler centroid of the $n^{\rm th}$ receiver, f_r is the pulse repetition frequency and $B_{d,\mathrm{Rx}}$ is the Doppler bandwidth of a single receiver.

The azimuth ambiguity is different for the case when narrow beams are used to synthesize the wide transmit beams. The azimuth ambiguity in this case consists of two components. The first component is the same as the conventional SISO SAR while the second component is due to the echoes which are transmitted by the other beams. The azimuth ambiguity to signal ratio in this case can be expressed as follows,

$$\mathrm{AASR}_n = \frac{P_{n,\mathrm{ambig}}}{P_{n,\mathrm{sig}}} \tag{51}$$

where,

$$P_{n,\mathrm{ambig}} = \sum_{\substack{k=-\infty\\k\neq 0}}^{\infty}\Big[\int_{(f_{dc,n}-0.5B_{d,\mathrm{Rx}})}^{(f_{dc,n}+0.5B_{d,\mathrm{Rx}})} G_{r,n}^2(f+kf_r)\mathrm{d}f + \sum_{m\neq n}\int_{(f_{dc,n}-0.5B_{d,\mathrm{Rx}})}^{(f_{dc,n}+0.5B_{d,\mathrm{Rx}})} G_{r,n}(f+kf_r)G_{r,m}(f+kf_r)\Delta_{nm}\mathrm{d}f\Big], \tag{52}$$

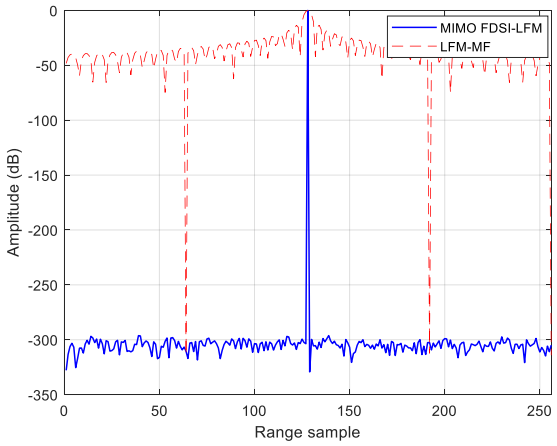

Fig. 3. The normalised point spread function of MIMO-FDSI method and LFM-MF method

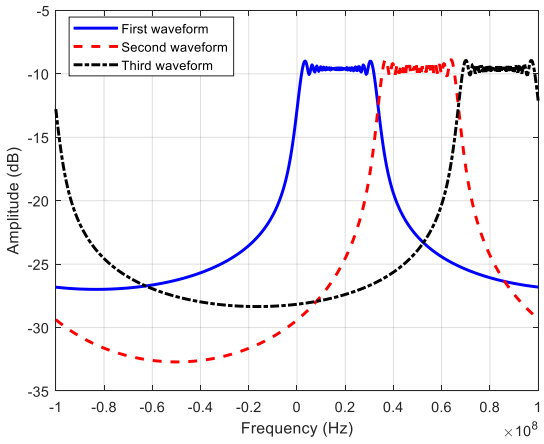

Fig. 4. The spectra of the transmitted waveforms

$$P_{n,\text{sig}} = \int_{(f_{dc,n}-0.5B_{d,\text{Rx}})}^{(f_{dc,n}+0.5B_{d,\text{Rx}})} G_{r,n}^2(f)\mathrm{d}f + \sum_{m\neq n}\int_{(f_{dc,n}-0.5B_{d,\text{Rx}})}^{(f_{dc,n}+0.5B_{d,\text{Rx}})} G_{r,n}(f)G_{r,m}(f)\Delta_{nm}\mathrm{d}f \quad (53)$$

$$\Delta_{nm}(r) = \frac{\int_{(m-n)t_d-\tau_p/2}^{(m-n)t_d+\tau_p/2} G_{el}^2(t-2r/c)\mathrm{d}t}{\int_{-\tau_p/2}^{\tau_p/2} G_{el}^2(t-2r/c)\mathrm{d}t}, \quad n\neq m \quad (54)$$

τ_p is the transmitted sub-pulse width, r is the slant range, G_{el} denotes the receiving elevation antenna pattern and Δ_{nm} is a reduction factor caused by the inter-beams suppression (IBS) operation [25]. According to [6], it is sufficient to shape the receiving elevation beam such that the range ambiguities remain below a given level (i.e. -25dB).

III. Simulation Results

The following section shows the numerical results of our proposed FDSI estimation algorithm for MIMO SAR using a set of LFM waveforms and compares it with a conventional SISO SAR using an LFM waveform. It is divided into four subsections in which the first subsection demonstrates the performance of range profile reconstruction while the second subsection shows how the azimuth ambiguity is avoided using the proposed MIMO SAR configuration. The third subsection illustrates the azimuth ambiguity characteristics for the case of different implementations of our proposed configuration and demonstrates how the side-lobes effect on the azimuth ambiguity is suppressed using IBS. The last subsection demonstrates the effectiveness of our proposed algorithm in a cluttered scene.

A. Performance of Range Profile Reconstruction

The point spread function (PSF) of the proposed method is compared with the point spread function of the conventional LFM waveform to illustrate the free inter-range cell interference property as shown in Fig.3 in which the proposed method exhibits ideally (i.e. the scatterer located at the exact sample time and the practical case is considered in III-B) a zero level side-lobes as the impulse response is measured directly unlike the case of the matched filter. The use of this scenario permits direct comparisons with the other IRCI-free approaches in the literature [17] [27] that consider the same scatterer location. It is assumed in the simulation that there are $M = 3$ transmit antennas, $N = 3$ receive antennas and the length of the channel impulse response is $L = 256$ which corresponds to the swath width. The distance between adjacent transmitters/receivers is assumed to be $1.5m$. Each transmit antenna emits a sub-band waveform with a bandwidth of $33.333MHz$ as shown in Fig.4. Accordingly, the total bandwidth of the received signal is $B_{tot} = M \times 33.333MHz = 100MHz$ and the range resolution of the system should be $1.5m$.

Consider next the case in which the length of the channel impulse response is $L = 700$ and a number of scatterers separated by $1.5m$ (i.e. range resolution) are present. The estimated impulse response is shown in Fig.5 for the case when $\text{SNR} = 10$dB. It is clear from the figure that the channel impulse response is perfectly recovered.

B. Azimuth Ambiguity Removal

Consider the simulation parameters listed in Table I and assume that the spectra of the emitted waveforms are as shown in Fig.4 and there is a single scatterer located at the swath centre. The MIMO configuration used in the simulation is as shown in Fig.1 in which the squint angles are $|\theta_2| = 0$ and $|\theta_1| = |\theta_3| = \theta_{BW}/N = 0.0148$ where θ_{BW} is the 3dB width of the wide transmit beam. The 3dB width of the conventional SISO SAR beam is θ_{BW} which is chosen to obtain the same cross-range resolution as the one in MIMO SAR. In addition, the azimuth and range cuts for the noiseless case are shown in Fig.6 and Fig.7, respectively. It is clear that there is no azimuth aliasing using our proposed algorithm even though the PRF used is lower than the Doppler bandwidth unlike the case in the conventional SISO SAR where aliased components are present.

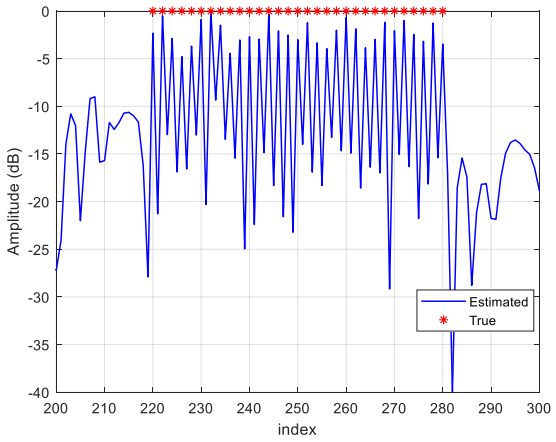

Fig. 5. Estimated channel impulse response for the case when a number of scatterers are present in the swath

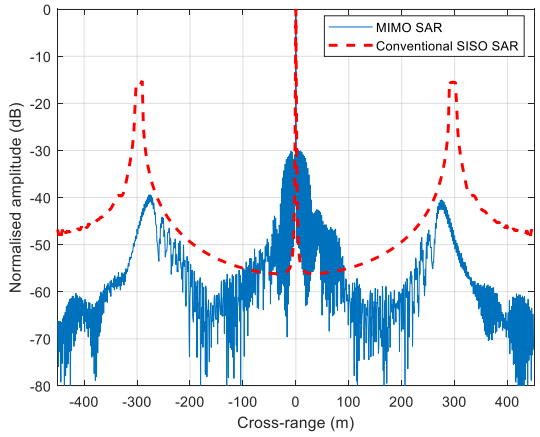

Fig. 6. The azimuth cut of the estimated scene using the proposed algorithm and the conventional SAR

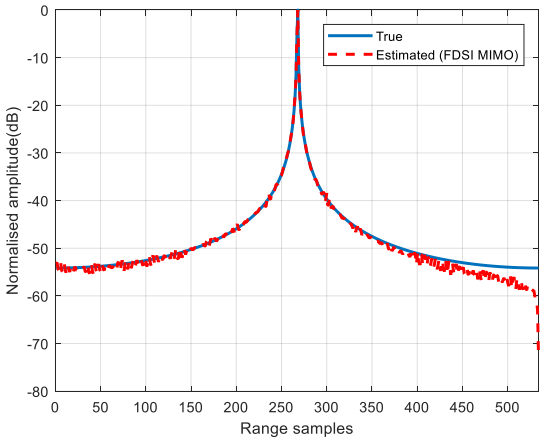

Fig. 7. The range cut of the true and estimated scene

TABLE I
SIMULATION PARAMETERS

Parameter	Symbol	Value
Number of Tx	M	3
Number of Rx	N	3
Min. distance to the swath centre	R_0	$20km$
Look angle	ϕ	45^o
Azimuth length of the conventional SISO SAR beamformer	L_a	$1.5m$
Azimuth length of the single beamformer in MIMO SAR	$L_{a,\mathrm{MIMO}}$	$4.5m$
Distance between adjacent Tx/Rx in MIMO SAR	d	$4.5m$
Doppler bandwidth	B_d	$300Hz$
Pulse repetition frequency	PRF	$100Hz$
Platform Velocity	v_p	$225m/s$
Carrier Frequency	F_c	$4.5GHz$
Sampling Frequency	F_s	$200MS/s$
Single waveform Bandwidth	BW	$33.333MHz$
Pulse width	τ	$2.5\mu s$

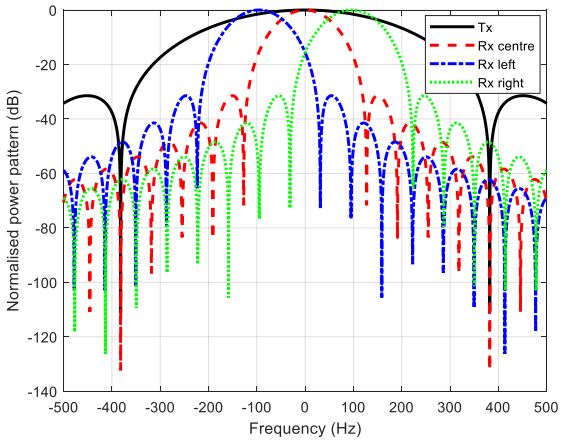

Fig. 8. The transmit and receive beam patterns as a function of frequency for the case when the proposed configuration is implemented using real wide transmit beams. It should be noted that all of the transmitters beams have the same shape.

C. Azimuth Ambiguity to Signal Ratio (AASR)

The azimuth ambiguity characteristics of the proposed MIMO SAR configuration implemented using real wide transmit beams and synthesised wide transmit beams are simulated and compared with the azimuth ambiguity of conventional SISO SAR based on the azimuth ambiguity to signal ratio (AASR). Assume that the beam patterns of the transmitters and receivers when the proposed configuration shown in Fig.1 is implemented using real wide transmit beams and synthesised wide transmit beams are as shown in Fig.8 and Fig.9, respectively. The beam pattern used in the conventional SISO SAR is the same as the Tx pattern in Fig.8 which has been chosen to obtain the same cross-range resolution as the one obtained in MIMO SAR.

The azimuth ambiguity to signal ratio (AASR) as a function of PRF of the proposed MIMO SAR configuration using the two different implementations is as shown in Fig.10 in which

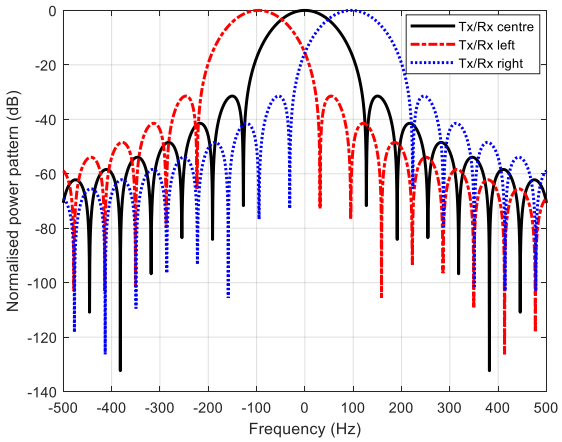

Fig. 9. The transmit and receive beam patters as a function of frequency for the case when the proposed configuration is implemented using synthesised wide transmit beams

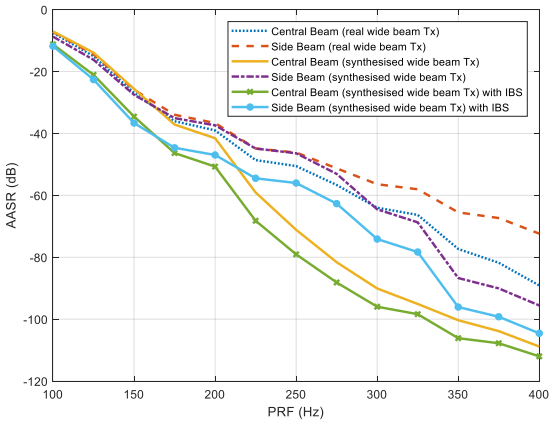

Fig. 10. Azimuth ambiguity characteristics of the proposed MIMO SAR implemented using real wide beams transmitters and synthesised wide beams transmitters. $\Delta_{nm} = -10$dB for the case of the inter-beam suppression (IBS)

only one of the side beams is considered because the other side beam has the same azimuth ambiguity characteristics. The azimuth ambiguity to signal ratio for the case of conventional SISO SAR is as shown in Fig.11 from which one can see that the PRF required for MIMO SAR configuration using any of the two different implementations is lower than that of conventional SISO SAR to attain the same azimuth ambiguity performance at the same cross-range resolution which makes it possible to have a wider swath.

It is clear from Fig.10 that the azimuth ambiguity characteristics of the proposed configuration using real wide beams transmitters are worse than that using synthesised beams. This is expected because the side-lobes of the receiving beams as shown in Fig.8 are located within the main-lobe of the wide transmit beam which would make the azimuth ambiguity stronger unlike the case of synthesised wide transmit beams implementation. The azimuth ambiguity characteristics of the side beams in both implementations are worse than that of the central beams and this is because the main-lobes of the side beams in the real wide beams transmitters implementation are located in the rolling-down part of the transmission main-lobe and many of the side-lobes of the receivers side-beams are located in the main-lobe peak part of the transmission beam which would make the azimuth ambiguity stronger. In addition, the power of the desired signal component (i.e. the second term of (53)) in the side beams of synthesised wide transmission beams implementation is lower than that of the central beam which would make the azimuth ambiguity characteristics worse. Furthermore, the azimuth ambiguity characteristics are better for the case of the synthesised wide beams with inter-beams suppression (IBS) because the second term of (52) is almost suppressed by digital beamforming on receiving in elevation. According to [28], the PRF should be chosen such that it is equal to an oversampling factor (1.1 to 1.4) multiplied by the 3dB Doppler bandwidth.

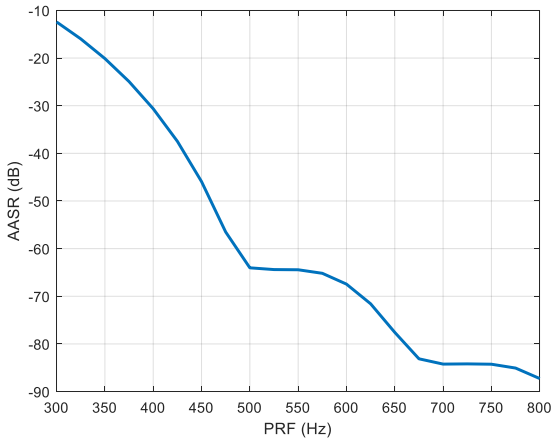

Fig. 11. Azimuth ambiguity characteristics of the conventional SISO SAR

D. Raw Data Simulation

As there is no multiple-phase centre FDMA MIMO SAR data available for us, a publicly available airborne SISO SAR data "Gotcha" [29] is used to construct MIMO SAR data to test our proposed FDSI-based algorithm in a cluttered scene. A way for constructing MIMO SAR data from raw conventional SISO SAR data has been used in the literature [30] under the assumption that all receivers have the same beams so that the received signals at all receivers occupy the same Doppler bandwidth.

In our proposed configuration, the received signals at each receiver occupy a portion of the total Doppler bandwidth which corresponds to the narrow receive beam. Accordingly, the first step of constructing MIMO SAR data is to divide the total azimuth angles into N parts because each single azimuth angle corresponds to a single Doppler frequency. The Doppler bandwidth of the received signals from each of the N parts corresponds to the Doppler bandwidth at one of the N receivers. Next, the following steps are performed on the

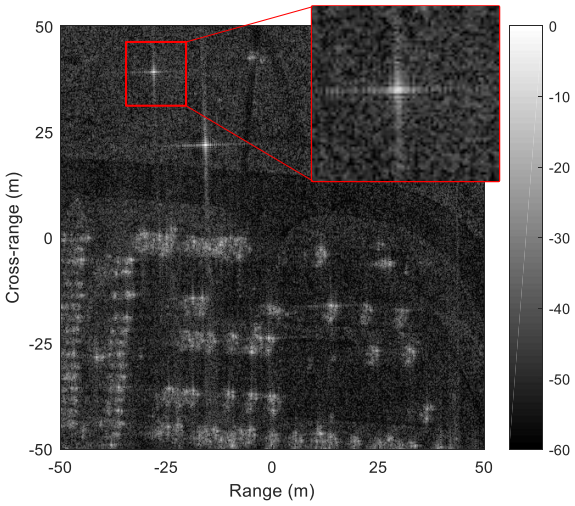

Fig. 12. Formed image using a single received data

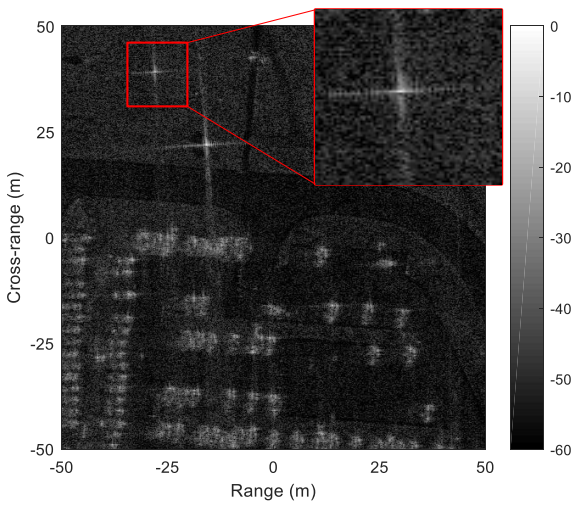

Fig. 13. Formed image using all receivers data

received signals at the n^{th} azimuth part which corresponds to the n^{th} receiver to construct the multiple-phase centre FDMA MIMO SAR data for the case when $M = N = 2$:

1) The data is transformed into range frequency domain.
2) The whole range bandwidth is divided into two sub-bands.
3) Each sub-band is transformed into Doppler domain and then multiplied by a slow time delay function to simulate the effective phase centre (EPC).
4) The data is then converted into range-azimuth domain and each sub-band data is convolved with the corresponding transmitted sub-band chirp.
5) The sub-bands data are added together to construct the MIMO SAR data received at the n^{th} receiver.

TABLE II
SYSTEM PARAMETERS

Parameter	Symbol	Value
Number of Tx	M	2
Number of Rx	N	2
Min. distance to the swath centre	R_0	$10.158km$
3dB width of a single MIMO receiver beamwidth	θ_{BW}	3^o
3dB width of the conventional SISO SAR	$\theta_{BW,\text{SISO}}$	6^o
Carrier Frequency	F_c	$9.58GHz$
distance between adjacent Tx/RX	d	$1m$
Single waveform Bandwidth	BW	$300MHz$

Consider the main system parameters listed in Table II. It should be noted that the inter-beams effect on the azimuth ambiguity is not considered here as it already has been addressed in Section III-C The formed image using the data received by a single receiver and the data combined from all receivers using the proposed algorithm are shown in Fig.12 and Fig.13, respectively. It is clear that the formed image using the data of all receivers has better cross-range resolution. In addition, the cross-range cuts of the indicated areas with red

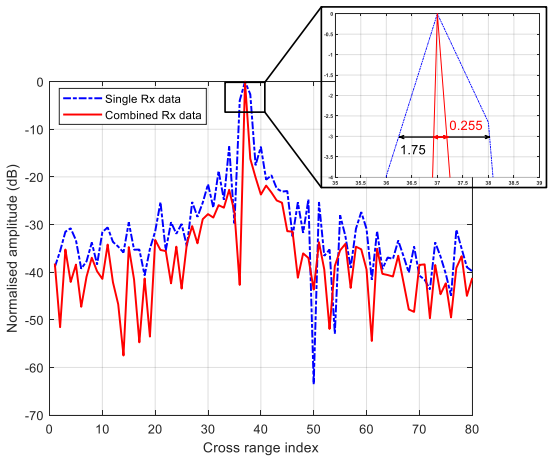

Fig. 14. The cross-range cuts of the indicated area with red rectangles in Fig.12 and Fig.13

rectangles in the formed images are shown in Fig.14 from which one can see that the cross-range resolution is improved using the combined data.

Next consider the case of the conventional SISO SAR in which the transmitted bandwidth is $300MHz$ and the sampling frequency across the azimuth is similar to MIMO SAR configuration. The formed image is as shown in Fig.15 where it is clear that the image is aliased. The sampling frequency across the azimuth should be double the one used in the MIMO SAR configuration in order to avoid the aliasing in the azimuth dimension. The formed image using double the sampling frequency of MIMO SAR is as shown in Fig.16. The range cuts of the indicated areas with red rectangles in the images shown in Fig.13 and Fig.16 are as shown in Fig.17. It is clear that the range resolution is better for the MIMO SAR configuration because it is possible to transmit more bandwidth and the narrowband assumption is relaxed to the bandwidth of the individual transmitting channel.

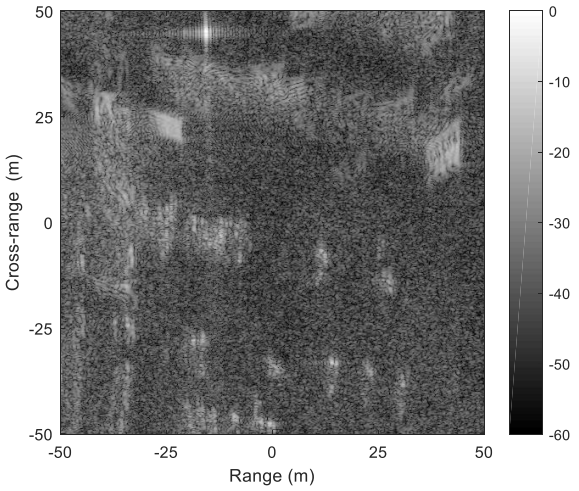

Fig. 15. Formed image using SISO SAR in which the azimuth sampling frequency is half the Doppler bandwidth and the same as the one used in MIMO SAR.

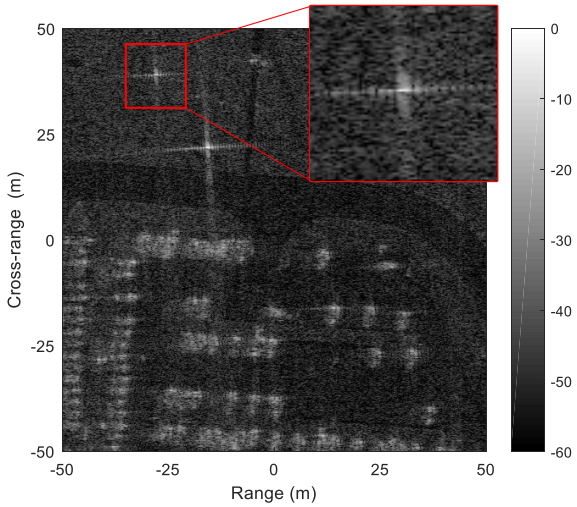

Fig. 16. Formed image using SISO SAR data in which the azimuth sampling frequency is double the one used in MIMO SAR.

IV. Conclusion

This paper presents an FDSI-MIMO SAR algorithm using multiple phase centre multiple azimuth beam to obtain high resolution wide swath imaging. The proposed algorithm is IRCI-free although no guard bands are added between the adjacent spectra of the transmitting waveforms (i.e. the spectra of transmitting waveforms are partially overlapped) which allowed us to utilise the available bandwidth to the maximum efficiency and the length of the waveform is not function of the channel impulse response in the range dimension which makes the proposed algorithm suitable for strip-map mode of operation. A set of conventional LFM waveforms is used for transmission to simplify implementations and hence gains all the inherent benefits of these waveforms (e.g. constant envelope and unity peak to average power). In addition, a PRF lower than the Doppler bandwidth is used to obtain wide swath without having aliasing in the Doppler spectrum. It is due to the multiple narrow azimuth beams formed on receiving. Wide transmission beams are synthesised using narrow beams in order to use the same antennas for both transmission and reception and achieve desired signal to noise ratio (SNR). The azimuth ambiguity characteristics of the proposed MIMO SAR configuration, implemented using real wide transmit beams and synthesised wide transmit beams, are analysed. Simulation results of point targets and constructed raw data are used to validate the effectiveness of the proposed algorithm.

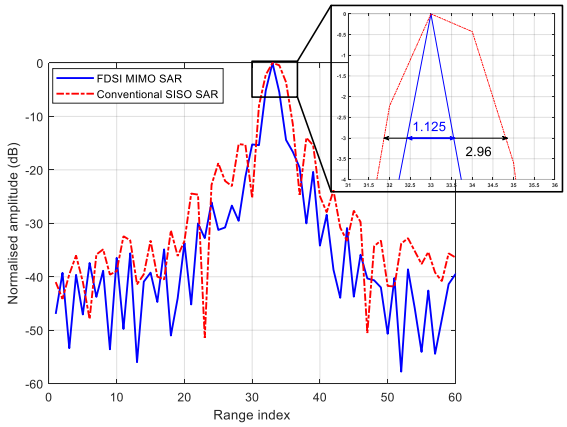

Fig. 17. The range cuts of the indicated area with red rectangles in Fig.13 and Fig.16.

Acknowledgment

The first author would like to acknowledge the support of King Abdulaziz City for Science and Technology (KACST) in Saudi Arabia.

Appendix A
Proof of the Round Trip Distance of a Scatterer

Assume that the signal is transmitted by the m^{th} transmitter and received by the n^{th} receiver which is located at $y = 0$ (the platform is moving along the y axis). We will need to prove that the following equation holds,

$$R_{l,m}(\eta) + R_{l,n}(\eta) \approx 2R_{l,m}(\eta - \frac{\Delta y_{mn}}{2v_p})_{\theta=\theta_n} + \frac{\Delta y_{mn}^2}{4R_l} \quad (55)$$

$R_{l,m}$ and $R_{l,n}$ can be expressed using (5) as the following (it should be noted that the squint angle of the transmitter will be the same as the squint angle of the receiver),

$$R_{l,m}(\eta) \approx R_l - v_p \sin(\theta_n)(\eta + \frac{\Delta y_{mn}}{v_p}) + \frac{v_p^2 \cos^2(\theta_n)(\eta + \Delta y_{mn}/(v_p))^2}{2R_l} \quad (56)$$

$$R_{l,n}(\eta) \approx R_l - v_p \sin(\theta_n)(\eta) + \frac{v_p^2 \cos^2(\theta_n)(\eta)^2}{2R_l} \quad (57)$$

The round trip distance of the l^{th} scatterer can be expressed as the following,

$$\begin{aligned} f(\eta) =& R_{l,m}(\eta) + R_{l,n}(\eta) \\ =& 2R_l - 2v_p\eta\sin(\theta_n) - v_p\sin(\theta_n)(\Delta y_{mn}/v_p) + \\ & \frac{v_p^2\cos^2(\theta_n)(\eta + \Delta y_{mn}/(v_p))^2}{2R_l} + \frac{v_p^2\cos^2(\theta_n)(\eta)^2}{2R_l} \end{aligned} \tag{58}$$

Quadratic approximation of (58) can be expressed as the following,

$$f(\eta) \approx f(0) + \acute{f}(0)\eta + \frac{1}{2}\acute{\acute{f}}(0)\eta^2 \tag{59}$$

$$f(0) = 2R_l - v_p\sin(\theta_n)(\Delta y_{mn}/v_p) + \frac{v_p^2\cos^2(\theta_n)(\Delta y_{mn}/v_p)^2}{2R_l} \tag{60}$$

$$\begin{aligned} \acute{f}(\eta) =& -2v_p\sin(\theta_n) + \frac{2v_p^2\cos^2(\theta_n)(\eta + \Delta y_{mn}/v_p)}{2R_l} \\ & + \frac{2v_p^2\cos^2(\theta_n)\eta}{2R_l} \end{aligned} \tag{61}$$

$$\acute{f}(0) = -2v_p\sin(\theta_n) + \frac{2v_p^2\cos^2(\theta_n)(\Delta y_{mn}/v_p)}{2R_l} \tag{62}$$

$$\acute{\acute{f}}(\eta) = \frac{2v_p^2\cos^2(\theta_n)}{R_l} = \acute{\acute{f}}(0) \tag{63}$$

Substituting (60)-(63) into (59),

$$\begin{aligned} f(\eta) \approx& 2R_l - v_p\sin(\theta_n)(\Delta y_{mn}/v_p) - 2v_p\eta\sin(\theta_n) \\ & + \frac{v_p^2\cos^2(\theta_n)}{R_l}\left(\frac{1}{2}(\frac{\Delta y_{mn}}{v_p})^2 + (\frac{\Delta y_{mn}}{2v_p})^2 - (\frac{\Delta y_{mn}}{2v_p})^2 + \right. \\ & \left. 2(\frac{\Delta y_{mn}}{2v_p})\eta + \eta^2\right) \end{aligned} \tag{64}$$

$$\begin{aligned} \approx& 2R_l - v_p\sin(\theta_n)(\Delta y_{mn}/v_p) - 2v_p\eta\sin(\theta_n) + \\ & \frac{v_p^2\cos^2(\theta_n)}{R_l}(\frac{1}{4}(\frac{\Delta y_{mn}}{v_p})^2 + (\eta + \frac{\Delta y_{mn}}{2v_p})^2) \end{aligned} \tag{65}$$

$$\approx 2R_{l,m}(\eta - \frac{\Delta y_{mn}}{2v_p})_{\theta=\theta_n} + \frac{(\Delta y_{mn}\cos(\theta_n))^2}{4R_l} \tag{66}$$

$$\approx 2R_{l,n}(\eta + \frac{\Delta y_{mn}}{2v_p})_{\theta=\theta_n} + \frac{(\Delta y_{mn}\cos(\theta_n))^2}{4R_l} \tag{67}$$

As the squint angles of the receivers are generally small, the following can be used,

$$\frac{(\Delta y_{mn}\cos(\theta_n))^2}{4R_l} \approx \frac{(\Delta y_{mn})^2}{4R_l} \tag{68}$$

Therefore,

$$\begin{aligned} f(\eta) =& R_{l,m}(\eta) + R_{l,n}(\eta) \\ \approx& 2R_{l,m}(\eta - \frac{\Delta y_{mn}}{2v_p})_{\theta=\theta_n} + \frac{(\Delta y_{mn})^2}{4R_l} \end{aligned} \tag{69}$$

$$\approx 2R_{l,n}(\eta + \frac{\Delta y_{mn}}{2v_p})_{\theta=\theta_n} + \frac{(\Delta y_{mn})^2}{4R_l} \tag{70}$$

Consider the geometry shown in Fig.1, the round trip distances can be expressed using (69) and (70) as the following,

$$R_{l,1}(\eta) + R_{l,2}(\eta) \approx 2R_{l,1}(\eta - \frac{d}{2v_p})_{\theta=\theta_{\text{Rx}}} + \frac{(d)^2}{4R_l} \tag{71}$$

$$\approx 2R_{l,2}(\eta + \frac{d}{2v_p})_{\theta=\theta_{\text{Rx}}} + \frac{(d)^2}{4R_l} \tag{72}$$

$$R_{l,2}(\eta) + R_{l,3}(\eta) \approx 2R_{l,2}(\eta - \frac{d}{2v_p})_{\theta=\theta_{\text{Rx}}} + \frac{(d)^2}{4R_l} \tag{73}$$

$$\approx 2R_{l,3}(\eta + \frac{d}{2v_p})_{\theta=\theta_{\text{Rx}}} + \frac{(d)^2}{4R_l} \tag{74}$$

$$R_{l,1}(\eta) + R_{l,3}(\eta) \approx 2R_{l,2}(\eta)_{\theta=\theta_{\text{Rx}}} + \frac{(d)^2}{R_l} \tag{75}$$

The azimuth impulse responses expressed in (8)-(12) can be obtained by substituting (71)-(75) into (7).

APPENDIX B
ILLUSTRATION OF A CIRCULANT MATRIX

The matrix $\mathbf{B}_{s,1C}(f_a)$ is as illustrated in (76).

REFERENCES

[1] N. Gebert, G. Krieger, and M. A. Moreira, "Digital beamforming on receive: Techniques and optimization strategies for high-resolution wide-swath SAR imaging," *IEEE Transactions on Aerospace and Electronic Systems*, vol. 45, no. 2, pp. 564–592, 2009.

[2] G. Min, W. Xiaoming, and H. Shunji, "Performance improvements in MIMO SAR," in *2008 IEEE Radar Conference, RADAR 2008*, 2008.

[3] J. H. G. Ender and J. Klare, "System architectures and algorithms for radar imaging by MIMO-SAR," in *IEEE National Radar Conference - Proceedings*, 2009.

[4] W. Q. Wang, "Space-time coding MIMO-OFDM SAR for high-resolution imaging," *IEEE Transactions on Geoscience and Remote Sensing*, vol. 49, no. 8, pp. 3094–3104, 2011.

[5] W. Xu, P. P Huang, and Y.-K. Deng, "Multi-channel SPCMB-tops SAR for High-Resolution Wide-Swath Imaging," *Progress In Electromagnetics Research*, vol. 116, 2011.

[6] G. Krieger, N. Gebert, and A. Moreira, "Multidimensional waveform encoding: A new digital beamforming technique for synthetic aperture radar remote sensing," *IEEE Transactions on Geoscience and Remote Sensing*, 2008.

[7] W. Xu, Y. Deng, and R. Wang, "Multichannel synthetic aperture radar systems with a planar antenna for future spaceborne microwave remote sensing," *IEEE Aerospace and Electronic Systems Magazine*, 2012.

[8] G. Krieger, N. Gebert, and A. Moreira, "High-resolution synthetic aperture side view radar system used by means of digital beamforming," 2007.

[9] R. Yang, H. Li, S. Li, P. Zhang, L. Tan, X. Gao, and X. Kang, *High-Resolution Microwave Imaging*, 2018.

[10] G. Krieger, "MIMO-SAR: Opportunities and pitfalls," *IEEE Transactions on Geoscience and Remote Sensing*, vol. 52, no. 5, pp. 2628–2645, 2014.

[11] W. Q. Wang, "Mitigating range ambiguities in high-PRF SAR with OFDM waveform diversity," *IEEE Geoscience and Remote Sensing Letters*, vol. 10, no. 1, pp. 101–105, 2013.

[12] W. Q. Wang and J. Cai, "Ground moving target indication by MIMO SAR with multi-antenna in azimuth," in *International Geoscience and Remote Sensing Symposium (IGARSS)*, 2011, pp. 1662–1665.

[13] H. Sun, F. Brigui, and M. Lesturgie, "Analysis and Comparison of MIMO Radar Waveforms," in *2014 International Radar Conference, Radar 2014*, 2014.

[14] J. P. Stralka, R. M. Thompson, J. Scanlan, and A. Jones, "MISO Radar Beamforming Demonstration," in *IEEE National Radar Conference - Proceedings*, 2011.

[15] P. P. Vaidyanathan and P. Pal, "MIMO radar, SIMO radar, and IFIR radar: A comparison," in *Conference Record - Asilomar Conference on Signals, Systems and Computers*, 2009.

$$\mathbf{B}_{s,1C}(f_a) =$$

$$\begin{bmatrix}
b_{s,1}[0,f_a] & \dots & 0 & \dots & 0 & & b_{s,1}[2,f_a] & b_{s,1}[1,f_a] \\
b_{s,1}[1,f_a] & \ddots & 0 & & 0 & \ddots & \vdots & b_{s,1}[2,f_a] \\
\vdots & & b_{s,1}[0,f_a] & & \vdots & \ddots & b_{s,1}[K-1,f_a] & \vdots \\
b_{s,1}[K-1,f_a] & \vdots & b_{s,1}[1,f_a] & \ddots & 0 & \vdots & 0 & b_{s,1}[K-1,f_a] \\
0 & & \vdots & & b_{s,1}[0,f_a] & \vdots & 0 & 0 \\
0 & \ddots & b_{s,1}[K-1,f_a] & \vdots & b_{s,1}[1,f_a] & \ddots & \vdots & 0 \\
\vdots & & 0 & \ddots & \vdots & \vdots \ddots & 0 & \vdots \\
 & & \vdots & & & \vdots & b_{s,1}[0,f_a] & 0 \\
0 & \dots & 0 & 0 & b_{s,1}[K-1,f_a] & & b_{s,1}[1,f_a] & b_{s,1}[0,f_a]
\end{bmatrix} \tag{76}$$

[16] Y. H. Cao and X. G. Xia, "IRCI-Free MIMO-OFDM SAR Using Circularly Shifted Zadoff-Chu Sequences," *IEEE Geoscience and Remote Sensing Letters*, vol. 12, no. 5, pp. 1126–1130, 2015.

[17] T. Zhang, X. G. Xia, and L. Kong, "IRCI free range reconstruction for SAR imaging with arbitrary length OFDM pulse," *IEEE Transactions on Signal Processing*, 2014.

[18] X. Luo, R. Wang, Y. Deng, and W. Xu, "Influences of channel errors and interference on the OFDM-MIMO SAR," in *2013 IEEE Radar Conference (RadarCon13)*, 2013, pp. 1–5.

[19] G. Jing, G. Sun, X. Xia, M. Xing, and Z. Bao, "A Novel Two-Step Approach of Error Estimation for Stepped-Frequency MIMO-SAR," *IEEE Geoscience and Remote Sensing Letters*, vol. 14, no. 12, pp. 2290–2294, 2017.

[20] M. AlShaya, M. Yaghoobi, and B. Mulgrew, "Multiple-Beam IRCI-Free MIMO SAR," in *2019 International Radar Conference (Radar)*, Toulon, 2019.

[21] ——, "Frequency Domain System Identification for High Resolution IRCI-Free Collocated MIMO Radar," in *The 15th European Radar Conference*, Madrid, 2018.

[22] A. Moreira, J. Mittermayer, and R. Scheiber, "Extended chirp scaling algorithm for air- and spaceborne SAR data processing in stripmap and ScanSAR imaging modes," *IEEE Transactions on Geoscience and Remote Sensing*, vol. 34, no. 5, pp. 1123–1136, 1996.

[23] N. Gebert, G. Krieger, and A. Moreira, "Multichannel azimuth processing in ScanSAR and TOPS mode operation," *IEEE Transactions on Geoscience and Remote Sensing*, 2010.

[24] M. Suess, B. Grafmueller, and R. Zahn, "A novel high resolution, wide swath SAR system," 2002.

[25] W. Xu, W. Xu, and Y. Deng, "Multichannel SAR With Reflector Antenna for High-Resolution Wide-Swath Imaging," *IEEE Antennas and Wireless Propagation Letters*, 2010.

[26] A. Currie and M. Brown, "Wide-swath SAR," *IEE Proceedings F Radar and Signal Processing*, 2010.

[27] T. Zhang and N. G. Xia, "OFDM synthetic aperture radar imaging with sufficient cyclic prefix," *IEEE Transactions on Geoscience and Remote Sensing*, 2015.

[28] I. G. Cumming and W. F. H., *Digital Processing of Synthetic Aperture Radar Data: Algorithms and implementation*. Boston: Artech House, 2005.

[29] "No Title." [Online]. Available: https://www.sdms.afrl.af.mil/

[30] M. Xing, Z. Bao, F. Zhou, J. Zhang, and G. Sun, "An Efficient Signal Reconstruction Algorithm for Stepped Frequency MIMO-SAR in the Spotlight and Sliding Spotlight Modes," *International Journal of Antennas and Propagation*, 2014.